

A Fourier-series-based Virtual Fields Method for the identification of 2-D stiffness distributions

T. T. Nguyen¹, J. M. Huntley¹, I. A. Ashcroft², P. D. Ruiz¹ and F. Pierron³

1. Loughborough University, Wolfson School of Mechanical and Manufacturing Engineering, Loughborough LE11 3TU, UK.

2. University of Nottingham, Faculty of Engineering, Nottingham NG7 2RD, UK.

3. University of Southampton, Faculty of Engineering and the Environment, Highfield, Southampton SO17 1BJ, UK.

Abstract

The Virtual Fields Method (VFM) is a powerful technique for the calculation of spatial distributions of material properties from experimentally-determined displacement fields. A Fourier-series-based extension to the VFM (the F-VFM) is presented here, in which the unknown stiffness distribution is parameterised in the spatial frequency domain rather than in the spatial domain as used in the classical VFM. We present in this paper the theory of the F-VFM for the case of elastic isotropic thin structures with known boundary conditions. An efficient numerical algorithm based on the 2-D fast Fourier transform is presented, which reduces the computation time by 3-4 orders of magnitude compared to a direct implementation of the F-VFM for typical experimental dataset sizes. Artefacts specific to the F-VFM (ringing at the highest spatial frequency near to modulus discontinuities) can be largely removed through the use of appropriate filtering strategies. Reconstruction of stiffness distributions with the F-VFM has been validated on three stiffness distribution scenarios under varying levels of noise in the input displacement fields. Robust reconstructions are achieved even when the displacement noise is higher than in typical experimental fields.

Keywords: Virtual Fields Method, inverse method, stiffness identification, Fourier series.

1. Introduction

Inverse problems may arise in solid mechanics when the knowledge of either the material properties (i.e., the constitutive equations, or parameters in those equations) or of the boundary conditions is restricted. Material parameters are often determined by implementing several standardised tests with the assumption that the stress or strain distributions within the testing region are uniform and/or known *a priori*. However, if the materials under test exhibit spatial variations in these parameters, this approach is no longer viable.

A significant volume of research has been carried out to solve inverse problems of this type. One approach for the linear elastic case is to solve for the modulus *analytically* while exploiting the information from elastography [1]. Exact distributions of the shear modulus valid for two-dimensions (2-D) and three-dimensions (3-D) are achieved up to a constant, by solving the momentum equation written for compressible elastic materials, given static (or time-dependent) full-field displacements $\mathbf{u}(x, y)$, the density $\rho(x, y)$ and the Lamé parameter $\lambda(x, y)$. If the Lamé parameter is not provided but the Poisson's ratio $\nu(x, y)$ is available, the shear modulus distribution can also be determined. The method is limited by its instability when applied to nearly-incompressible materials and by its high sensitivity to noise as it requires derivatives of strains. The method is also not suitable for large deformation problems, for example those involving hyperelasticity material models. Incompressible isotropic plane stress inverse problems can be solved to within an unknown scaling constant using a variational method related to least squares, but with weighting by the adjoint operator [2].

Finite element model updating (FEMU) is another method to solve inverse problems by adjusting an approximate finite element model until the responses it produces are as close to those acquired from experiments as possible. In other words FEMU will update the numerical model iteratively while minimising the residual (also known as the *cost function*), the difference between a measured and computed measurand, in a least-squares sense. Experimental data can be either static (static deformed shape) [3, 4] or dynamic (natural frequencies or mode shapes) [5, 6]. The confidence of the results obtained from a FEMU scheme may depend on (i) the closeness of the numerical model to the real experiment where, for example, boundary conditions may not be well defined; (ii) the cost and available run time of the computational facilities; (iii) the convergence ability of the optimisation algorithm being used (which in turn is dependent on the initial parameter estimates, the lower/upper bounds of the design variables, etc.); and (iv) the sensitivity of the method to noisy data. A state-of-the-art review of the FEMU, together with several of other inverse methods, can be read in [7].

An alternative approach to tackling inverse problems of this kind is by using the virtual fields method (VFM). The development of the VFM was inspired by a relevant interpretation of the equation of the virtual work principle [8]. The advantage of the VFM compared to the FEMU technique is its ability to solve inverse problems of this type without any iteration. Numerous

applications of the VFM to date can be found in [8]. The key feature in any application of the VFM is the selection of the virtual fields. Several techniques based on different choices of virtual fields have been presented [9-12]. The common point of these techniques is the selection of the virtual fields as polynomials of spatial variables (either on the whole domain or in a piecewise form), and the material properties are considered as having single values (homogeneous) within the domain. The first attempt to parameterise the material properties as a function of spatial variables was proposed recently in [13] where the authors tried to reconstruct the spatial-dependent stiffness map of a plate with impact damage.

In this paper, we retain the basic concepts underlying the VFM but approach the parameterisation of the material properties in the spatial frequency, rather than spatial, domain by performing a 2-D Fourier series expansion of the stiffness distribution over the region of interest. Furthermore, the virtual fields are not selected as polynomials of spatial variables as in the previous VFM literature, but from a set of simple cosine or sine functions of different spatial frequencies. The VFM with a Fourier series for the material property parameterisation and cosine/sine functions for the virtual fields will be denoted the F-VFM throughout this paper. The F-VFM has been successfully applied to challenging stiffness distribution scenarios when the boundary conditions are specified.

The paper is structured as follows. The mathematical implementation of the F-VFM is presented in Section 2 followed by a demonstration of the method with numerical data in Section 3. The effect of the noise on the performance of the newly developed method is investigated in Section 4 by introducing different white noise levels into the kinematic data. Further discussions of the method and conclusions can be found in Section 5.

2. Principle of the Fourier-series-based Virtual Fields Method in two dimensions

2.1. Parameterisation of the stiffness distribution by a 2-D Fourier series expansion

The fundamental equation of the VFM is replicated from the principle of virtual work (PVW) equation (integral form) written for a deformable body, which describes the balance between the virtual works of internal and external forces with any C^0 (continuous and differentiable) virtual displacement field (and its associated virtual strain field). In the case of a 2-D thin structure with the assumptions that the volume force applied to the body is small enough to be neglected, and the structure is under plane stress conditions, the equilibrium equation of the structure can be written as in [11],

$$-\int_S \boldsymbol{\epsilon}^* \mathbf{Q} \boldsymbol{\epsilon} dS + \int_{\ell} \mathbf{T} \mathbf{u}^* d\ell = 0. \quad (1)$$

The definitions of the various terms in equation (1) are as follows:

S : area of interest within the structure over which the experimental data are available,

ℓ : part of the boundary of (S) on which tractions exist,

\mathbf{Q} : reduced stiffness matrix of size 3×3 specifying the material properties of the structure,

$\boldsymbol{\epsilon}$: vector of measured strain fields over (S) ; $\boldsymbol{\epsilon} = (\epsilon_{xx}, \epsilon_{yy}, \epsilon_{ss})'$, where ϵ_{xx} and ϵ_{yy} are the normal strains as measured along x - and y -axes of a Cartesian coordinate system, and ϵ_{ss} the engineering shear strain ($\epsilon_{ss} = 2\epsilon_{xy}$),

\mathbf{T} : vector of tractions defined over (ℓ) ; $\mathbf{T} = (T_x, T_y)$,

$\mathbf{u}^*, \boldsymbol{\epsilon}^*$: vectors of virtual displacement and virtual strain fields respectively; $\mathbf{u}^* = (u_x^*, u_y^*)'$, $\boldsymbol{\epsilon}^* = (\epsilon_{xx}^*, \epsilon_{yy}^*, \epsilon_{ss}^*)$.

Equation (1) will be true if the chosen virtual displacement field is continuous and differentiable (C^0 continuity) (see [8] for a detailed description of the principle of the VFM in 2-D).

Figure 1. A thin structure of arbitrary shape subject to a traction distribution \mathbf{T} on a portion (ℓ) of the boundary.

In the in-plane linear elastic orthotropic case, the four components $(Q_{xx}, Q_{yy}, Q_{xy}, Q_{ss})$ of the reduced stiffness matrix \mathbf{Q} are independent [14], i.e.

$$\mathbf{Q} = \begin{pmatrix} Q_{xx} & Q_{xy} & 0 \\ Q_{xy} & Q_{yy} & 0 \\ 0 & 0 & Q_{ss} \end{pmatrix} = \begin{pmatrix} \frac{E_{xx}}{1-\nu_{xy}\nu_{yx}} & \frac{\nu_{xy}E_{yy}}{1-\nu_{xy}\nu_{yx}} & 0 \\ \frac{\nu_{xy}E_{yy}}{1-\nu_{xy}\nu_{yx}} & \frac{E_{yy}}{1-\nu_{xy}\nu_{yx}} & 0 \\ 0 & 0 & G_{xy} \end{pmatrix}, \quad (2)$$

where E_{ii} is the elastic modulus along direction i ; ν_{ij} the Poisson's ratio representing the deformation in direction j when a load is applied in direction i (where $i, j = x$ or y); and G_{xy} the shear modulus. The reduced stiffness matrix in plane-stress isotropic case is dependent on only two stiffness components Q_{xx} and νQ_{xx} [14], with ν the Poisson's ratio, as

$$\mathbf{Q} = \begin{pmatrix} Q_{xx} & \nu Q_{xx} & 0 \\ \nu Q_{xx} & Q_{xx} & 0 \\ 0 & 0 & \frac{1-\nu}{2} Q_{xx} \end{pmatrix} = \frac{E}{1-\nu^2} \begin{pmatrix} 1 & \nu & 0 \\ \nu & 1 & 0 \\ 0 & 0 & \frac{1-\nu}{2} \end{pmatrix}. \quad (3)$$

where Q_{xx} is related to ν and the usual Young's modulus E through

$$Q_{xx} = \frac{E}{1-\nu^2} \quad (4)$$

Note that even in the isotropic case, the concept of 'stiffness' will still be used instead of 'modulus' to allow for a more convenient extension to either orthotropic or anisotropic situations where the modulus is dependent on direction.

Equation (1) can therefore be reformulated for a linear elastic isotropic body over its domain limited within the boundary (S) as

$$\int_S (\epsilon_{xx}^* \quad \epsilon_{yy}^* \quad \epsilon_{ss}^*) \begin{pmatrix} Q_{xx} & \nu Q_{xx} & 0 \\ \nu Q_{xx} & Q_{xx} & 0 \\ 0 & 0 & \frac{1-\nu}{2} Q_{xx} \end{pmatrix} \begin{pmatrix} \epsilon_{xx} \\ \epsilon_{yy} \\ \epsilon_{ss} \end{pmatrix} dS = \int_{\ell} (T_x \quad T_y) \begin{pmatrix} u_x^* \\ u_y^* \end{pmatrix} d\ell \quad (5)$$

i.e.

$$\begin{aligned} \int_S \left(\left(\epsilon_{xx}^* \epsilon_{xx} + \epsilon_{yy}^* \epsilon_{yy} + \frac{1}{2} \epsilon_{ss}^* \epsilon_{ss} \right) + \nu \left(\epsilon_{xx}^* \epsilon_{yy} + \epsilon_{yy}^* \epsilon_{xx} - \frac{1}{2} \epsilon_{ss}^* \epsilon_{ss} \right) \right) Q_{xx} dS \\ = \int_{\ell} (T_x u_x^* + T_y u_y^*) d\ell \end{aligned} \quad (6)$$

The early VFM was based on the assumption that the stiffness distribution (e.g. Q_{xx} in Eqn. (6)) is uniform over the domain (S), allowing it to be taken outside the integral on the left-hand side of Eqn (6). The integrand then only includes the measured and virtual deformation fields, which leads to a direct computation of the stiffness when the tractions on the right hand side are known [10]. However, this single-value-stiffness assumption is only acceptable for macro-scale observations where the structures are considered homogeneous. As the material is generally not homogeneous on the meso- and micro-scales, a continuous parameterisation technique of representing the stiffness components as polynomials of the spatial variables was proposed in [13]. In this way, the coefficients of the polynomials will be isolated from the integral, as desired. Recently, a discrete parameterisation method of the VFM has been proposed and successfully applied in 2-D [15], 3-D [16] and to welds [17-19].

In this paper, as previously stated, we approach the stiffness parameterisation from a different direction: instead of expressing the stiffness distributions as polynomials, we write them as Fourier series of spatial variables (x, y). In the simplest form, where ν is approximated as a known position-independent constant, Q_{xx} may be written as follows:

$$Q_{xx}(x, y) = \sum_{m=0}^N \sum_{n=-N}^N a_{m,n} \cos 2\pi \left(\frac{mx}{L_x} + \frac{ny}{L_y} \right) + \sum_{m=0}^N \sum_{\substack{n=-N \\ m+|n| \neq 0}}^N b_{m,n} \sin 2\pi \left(\frac{mx}{L_x} + \frac{ny}{L_y} \right) \quad (7)$$

where L_x and L_y are the dimensions of the 2-D domain (S); (x, y) the coordinates of all the points within boundary (S) over which experimental data is available; $a_{m,n}$, $b_{m,n}$ the Fourier coefficients of the series with spatial frequencies components (m, n); and N the maximum value of both indices m and n . The presence of negative frequency coefficients (n) in Eqn. (7) needs a brief explanation. In a standard 2-D discrete Fourier transform, the lower limit for both m and n would be 0. Negative frequencies in that case are implicitly present as aliased high frequencies generated by m and n values lying above the Nyquist limit. In the current case, however, the upper limit of m and n in practice will lie well below the Nyquist frequency for typical strain field resolution. For example, for a 1000×1000 pixel strain field, we would require N to equal 1000 before all the negative frequencies could be generated in this way. The number of degrees of freedom would then become impractically large and in

practice, as will be seen in Section 3, we typically choose values of N equal to or less than 40. As a result, it is necessary for the general case to explicitly include the negative frequencies in the summation of Eqn. (7). However, due to the even/odd symmetry of the cosine/sine functions, only one of the two indices m and n needs to take negative values. In this case we have chosen index m to take the values from 0 to N whilst index n runs from $-N$ to N . The constraint $m + |n| \neq 0$ ensures that m and n in the sine part of the expansion cannot be zero at the same time, which would otherwise lead to a zero row in the coefficient matrix. In certain cases it may be permissible to omit the negative frequencies, i.e. the lower limit on the summation over n can be 0 rather than $-N$. This is the case for the first two applications of section 3, where the stiffness distributions contain a fairly limited range of spatial frequencies. However, the third application involving a stiff inclusion requires both positive and negative spatial frequencies. A lower limit on n of $-N$, as specified in Eqn. (7), was used in this case in order to avoid significant stiffness reconstruction artefacts.

The assumption that ν is a known constant is reasonable in many cases, but where it is not, a second Fourier series expansion of the variable νQ_{xx} can be performed. This leads to a second set of Fourier coefficients that need to be solved for as part of the analysis. In the orthotropic case one would need four separate Fourier series expansions, one for each of the independent stiffness matrix components Q_{xx} , Q_{yy} , Q_{xy} and Q_{ss} .

Equation (7) can also be represented in matrix form, with the use of a shorthand notation for cosine and sine functions with spatial frequency components (m, n) as $c_{m,n}(x, y) = \cos 2\pi \left(\frac{mx}{L_x} + \frac{ny}{L_y} \right)$ and $s_{m,n}(x, y) = \sin 2\pi \left(\frac{mx}{L_x} + \frac{ny}{L_y} \right)$ so that

$$\begin{aligned}
 Q_{xx}(x, y) &= \sum_{m=0}^N \sum_{n=-N}^N a_{m,n} c_{m,n}(x, y) + \sum_{m=0}^N \sum_{\substack{n=-N \\ m+|n| \neq 0}}^N b_{m,n} s_{m,n}(x, y) \\
 &= (1 \quad \dots c_{m,n}(x, y) \quad \dots \quad \dots s_{m,n}(x, y) \quad \dots) \begin{pmatrix} a_{0,0} \\ \vdots \\ a_{m,n} \\ \vdots \\ b_{m,n} \\ \vdots \end{pmatrix}
 \end{aligned} \tag{8}$$

Note that the first summation term on the right hand side of Eqn. (8) includes the dc coefficient $a_{0,0}$, whereas the second summation specifically excludes the $b_{0,0}$ coefficient as in a standard Fourier series of a 2-D function [20]. The total number of unknown Fourier coefficients in Eqn. (8) is

$$N_F = 2(N + 1)(2N + 1) - 1 \tag{9}$$

for the case where the lower limit on n in Eqns. (7) and (8) is $-N$, and

$$N_F = 2(N + 1)^2 - 1 \tag{10}$$

when the lower limit is 0.

By substituting Eqn. (8) into Eqn. (6), and denoting

$$P(x, y) = (\epsilon_{xx} + \nu\epsilon_{yy})\epsilon_{xx}^* + (\epsilon_{yy} + \nu\epsilon_{xx})\epsilon_{yy}^* + \frac{1-\nu}{2}\epsilon_{ss}\epsilon_{ss}^*, \quad (11)$$

Eqn. (6) becomes

$$\left(\int_S P dS \quad \dots \int_S P c_{m,n} dS \quad \dots \int_S P s_{m,n} dS \quad \dots \right) \begin{pmatrix} a_{0,0} \\ \vdots \\ a_{m,n} \\ \vdots \\ b_{m,n} \\ \vdots \end{pmatrix} = \int_{\ell} (T_x u_x^* + T_y u_y^*) d\ell. \quad (12)$$

The row vector on the left-hand side of Eqn. (12) consists of the components of the 2-D Fourier transform of $P(x, y)$. A particular choice of virtual field results in one equation of the form of Eqn. (12). This one equation by itself is sufficient to obtain only the simplest solution of a single Fourier coefficient, the dc term $a_{0,0}$, corresponding to the case $N = 0$. However, additional equations are obtainable by selecting different virtual fields, thus giving rise to different forms for the function $P(x, y)$. In what follows, $P^{(j)}(x, y)$ will be used to denote this function for the j -th virtual field. Its 2-D Fourier transform, and hence the row vector in Eqn. (12), as well as the right-hand-side scalar are also correspondingly modified. So long as at least N_F virtual fields are chosen to give N_F independent equations of the form of Eqn. (12), these can be assembled to give the matrix equation

$$\mathbf{M}\mathbf{X} = \mathbf{Y} \quad (13)$$

where

$$\mathbf{M} = \begin{pmatrix} \int_S P^{(1)} dS & \dots \int_S P^{(1)} c_{m,n} dS & \dots \int_S P^{(1)} s_{m,n} dS & \dots \\ \vdots & \vdots & \vdots & \vdots \\ \int_S P^{(N_F)} dS & \dots \int_S P^{(N_F)} c_{m,n} dS & \dots \int_S P^{(N_F)} s_{m,n} dS & \dots \end{pmatrix} \quad (14)$$

$$\mathbf{X} = \begin{pmatrix} a_{0,0} \\ \vdots \\ a_{m,n} \\ \vdots \\ b_{m,n} \\ \vdots \end{pmatrix} \quad (15)$$

$$\mathbf{Y} = \begin{pmatrix} \int_{\ell} (T_x u_x^{*(1)} + T_y u_y^{*(1)}) d\ell \\ \vdots \\ \int_{\ell} (T_x u_x^{*(N_F)} + T_y u_y^{*(N_F)}) d\ell \end{pmatrix} \quad (16)$$

Equation (13) can then be inverted to solve for the vector \mathbf{X} containing the required Fourier coefficients $a_{m,n}$ and $b_{m,n}$ that describe the stiffness distribution.

2.2. Selection of virtual displacement and strain fields

To find the coefficients of the Fourier series in Eqn. (8), different virtual displacement fields and their derivatives are necessary to build up the left-hand-side matrix in Eqn. (14). The choice of these virtual fields is the key issue in any VFM application as it will directly affect the degree of independence of the linear system of equations (Eqn. (13)). In earlier developments of the VFM, the potential virtual fields were selected on a trial-and-error basis to ensure that the equations of linear system Eqn. (13) are independent. Later, the stability of the linear system Eqn. (13) was improved by means of a special virtual fields selection strategy [10]. The selection can be implemented so that the integrals corresponding to the unknown stiffness components take their turn to be 0 or 1, so that matrix \mathbf{M} in Eqn. (14) becomes an identity matrix. Further development of the VFM included an optimal selection of the virtual fields which at the same time preserves the stability of the system of equations (Eqn. (13)) and reduces the sensitivity of the method to the noise [9]. The virtual displacements and strains in those studies are defined as continuous functions either over the whole domain or piecewise within its subdomains [12].

In the F-VFM, the natural choice for the virtual fields is an arrangement of simple cosine and sine functions. Eqn. (6) involves area integrals of terms of the form $\epsilon_{\alpha\alpha}^* \epsilon_{\beta\beta} Q_{xx}$ ($\alpha, \beta = x, y, s$); the use of different spatial frequencies in the virtual fields therefore allows a given spatial frequency in the measured strain field $\epsilon_{\beta\beta}$ to be linked in turn with different coefficients in the Fourier expansion of Q_{xx} .

No special optimised fields have been developed yet for the F-VFM, but a few simple rules have been used to select the virtual fields as follows:

1. The set of virtual field spatial frequencies should be the same as that for the modulus parameterization so that a given spatial frequency in the measured strain field $\epsilon_{\beta\beta}$ can be linked in turn with all the coefficients in the Fourier expansion of Q_{xx} ;
2. Each spatial frequency for a given virtual strain field component should have both a sine and cosine wave of unit amplitude to ensure that the signal in $\epsilon_{\beta\beta}$ at that spatial frequency is detected regardless of its phase;
3. The total number of virtual fields should be equal to N_F in order to determine uniquely the unknown Fourier series coefficients of Eqn. (8).

When selecting the virtual fields, one has a choice between defining u_x^* and u_y^* , from which the virtual strain components are obtained by differentiation, or defining ϵ_{xx}^* , ϵ_{yy}^* and ϵ_{ss}^* , from which the virtual displacement components are obtained by integration. The former approach was used here to ensure compatibility between the inter-related strain components. In the case of a tensile test with loading along the x axis, most of the signal resides in the ϵ_{xx} and ϵ_{yy} fields, and therefore (according to rule (2) above) the u_x^* and u_y^* fields should be selected to produce the unit amplitude sine/cosine waves in ϵ_{xx}^* and ϵ_{yy}^* . One approach would be to define a set of fields with u_x^* chosen to produce the unit waves in ϵ_{xx}^* , with u_y^* set to

zero, and then a second set of fields this time with the unit waves in ϵ_{yy}^* and with u_x^* set to zero. However, this choice results in $2N_F$ virtual fields which is twice the number required to satisfy rule (3) above. The approach taken here was therefore to define a set of fields with both u_x^* and u_y^* chosen to produce the unit waves in ϵ_{xx}^* and ϵ_{yy}^* simultaneously. Thus both the ϵ_{xx}^* and ϵ_{yy}^* fields consist of a set of cosine waves (with spatial frequency components (p, q) where $p = 0, 1, \dots, N$; $q = -N, \dots, N$ giving $(2N+1)(N+1)$ independent virtual fields), and a set of corresponding sine waves (in which the trivial case $p = q = 0$ is excluded, giving an additional $(2N+1)(N+1) - 1$ fields). The total number of chosen cosine and sine virtual fields will therefore be equal to N_F , which is the required number to determine uniquely the unknown Fourier series coefficients of Eqn. (8). An additional benefit resulting from this choice of virtual fields is that it allows a fast algorithm to be employed, based on 2-D fast Fourier transforms, as will be discussed in the next section.

It is convenient to write matrix \mathbf{M} from Eqn. (14) in terms of the sub-matrices \mathbf{A} , \mathbf{B} , \mathbf{C} and \mathbf{D} as follows

$$\mathbf{M} = \begin{pmatrix} \mathbf{A} & \mathbf{B} \\ \mathbf{C} & \mathbf{D} \end{pmatrix} \quad (17)$$

where \mathbf{A} is of size $(N+1)(2N+1)$ rows \times $(N+1)(2N+1)$ columns, \mathbf{B} is $(N+1)(2N+1) \times ((N+1)(2N+1) - 1)$, \mathbf{C} is $((N+1)(2N+1) - 1) \times (N+1)(2N+1)$, and \mathbf{D} is $((N+1)(2N+1) - 1) \times ((N+1)(2N+1) - 1)$. \mathbf{A} and \mathbf{C} contain the cosine terms $c_{m,n}$ in the stiffness expansion with \mathbf{B} and \mathbf{D} containing the sine terms $s_{m,n}$. \mathbf{A} and \mathbf{B} contain the corresponding cosine waves in ϵ_{xx}^* and ϵ_{yy}^* (denoted $c_{p,q}$) with \mathbf{C} and \mathbf{D} containing the sine terms $s_{p,q}$.

Before the system of equations given in Eqn. (13) can be solved, both the virtual shear strain field ϵ_{ss}^* and virtual displacement components u_x^* and u_y^* need to be specified. The cosine and sine terms for ϵ_{xx}^* and ϵ_{yy}^* can be integrated to give u_x^* and u_y^* , from which all the partial derivatives with respect to x and y can be obtained. The virtual strain fields are calculated from these derivatives as follows:

$$\begin{aligned} \epsilon_{xx}^* &= \frac{\partial u_x^*}{\partial x}, \\ \epsilon_{yy}^* &= \frac{\partial u_y^*}{\partial y}, \\ \epsilon_{ss}^* &= \frac{\partial u_x^*}{\partial y} + \frac{\partial u_y^*}{\partial x}. \end{aligned} \quad (18)$$

All the virtual displacement and displacement derivative terms, including the special cases $p = 0$ and $q = 0$, are summarized in Table **IError! Reference source not found.**

Table I. Virtual displacement field components u_x^* and u_y^* and their derivatives.

Combining Eqns. (11) and (18) and Table **IError! Reference source not found.**, we see that the contribution from the normal strains to the general term in matrix \mathbf{M} can be written

$$\begin{aligned}
& \int_S \left((\epsilon_{xx} + \nu \epsilon_{yy}) \epsilon_{xx}^* + (\epsilon_{yy} + \nu \epsilon_{xx}) \epsilon_{yy}^* \right) \{c_{m,n}\}_{s_{m,n}} dS \\
& = (1 + \nu) \int_S (\epsilon_{xx} + \epsilon_{yy}) \{c_{p,q}\}_{s_{p,q}} \times \{c_{m,n}\}_{s_{m,n}} dS
\end{aligned} \tag{19}$$

where the $\{ \cdot \} \times \{ \cdot \}$ notation indicates a product of a cosine/sine virtual strain field component with a cosine/sine term from the modulus expansion, the particular combination being dependent on the quadrant (**A**, **B**, **C** or **D**) of the **M** matrix. The shear strains can be expressed in similar form, as follows:

$$\begin{aligned}
& \frac{1 - \nu}{2} \int_S \epsilon_{ss}^* \epsilon_{ss} \{c_{m,n}\}_{s_{m,n}} dS \\
& = \begin{cases} \frac{1 - \nu}{2} \int_S \epsilon_{ss} \left(\frac{L_x q}{L_y p} + \frac{L_y p}{L_x q} \right) \{c_{p,q}\}_{s_{p,q}} \times \{c_{m,n}\}_{s_{m,n}} dS & (p \neq 0, q \neq 0) \\ \frac{1 - \nu}{2} \int_S x \epsilon_{ss} \left(\frac{2\pi q}{L_y} \right) \begin{Bmatrix} -s_{0,q} \\ c_{0,q} \end{Bmatrix} \times \{c_{m,n}\}_{s_{m,n}} dS & (p = 0) \\ \frac{1 - \nu}{2} \int_S y \epsilon_{ss} \left(\frac{2\pi p}{L_x} \right) \begin{Bmatrix} -s_{p,0} \\ c_{p,0} \end{Bmatrix} \times \{c_{m,n}\}_{s_{m,n}} dS & (q = 0) \end{cases}
\end{aligned} \tag{20}$$

2.3. Fast algorithm for the F-VFM

When applying equations (19) and (20) to experimental data, the measured strain fields ϵ_{xx} , ϵ_{yy} and ϵ_{ss} are normally sampled on a regular grid and the integrals are replaced by summations. If the experimental strain fields have $N_x \times N_y$ pixels, then a single contributory term to one of the elements of **M** requires a minimum of $N_x N_y$ addition plus multiplication operations. As **M** is non-sparse, the computational cost to calculate **M** therefore scales as $C_1 N_F^2$ where C_1 is $O(N_x N_y)$. For example, the second application given in the next section, with $N_x = N_y = 1000$ and $N_F = 881$ ($N = 20$), took approximately 5.5×10^3 s to set up the **M** matrix on an Intel® Core™ i7 CPU 2.79 GHz machine with 8GB of memory.

A much more efficient algorithm can be implemented, however, using 2-D fast Fourier transforms. The $\{ \cdot \} \times \{ \cdot \}$ term from Eqns. (19) and (20) can be rewritten as follows:

$$\begin{aligned}
c_{m,n} c_{p,q} &= \frac{1}{2} (c_{m+p,n+q} + c_{m-p,n-q}), \\
c_{m,n} s_{p,q} &= \frac{1}{2} (s_{m+p,n+q} - s_{m-p,n-q}), \\
s_{m,n} c_{p,q} &= \frac{1}{2} (s_{m+p,n+q} + s_{m-p,n-q}), \\
s_{m,n} s_{p,q} &= \frac{1}{2} (-c_{m+p,n+q} + c_{m-p,n-q}).
\end{aligned} \tag{21}$$

The right-hand side of Eqns. (19) and (20) all reduce to scaled versions of $\Re[H(j, k)]$ and $\Im[H(j, k)]$, respectively, where \Re and \Im denote real and imaginary parts of a complex variable, and H is given by

$$H(j, k) = \int_S h(x, y)(c_{j,k} - is_{j,k})dS \quad (22)$$

in which j and k are spatial frequency components, i is the square root of -1, and h is a function derived from the experimental strain fields.

In discrete form Eqn. (22) can be written

$$H(j, k) = \frac{L_x L_y}{N_x N_y} \sum_{\bar{x}=0}^{N_x-1} \sum_{\bar{y}=0}^{N_y-1} \bar{h}(\bar{x}, \bar{y})(\bar{c}_{j,k} - i\bar{s}_{j,k}) \quad (23)$$

where \bar{x} and \bar{y} are non-dimensional spatial coordinates ($\bar{x} = 0, 1, 2, \dots, N_x - 1$; $\bar{y} = 0, 1, 2, \dots, N_y - 1$), \bar{h} is h expressed in terms of these coordinates, and

$$\begin{aligned} \bar{c}_{j,k}(\bar{x}, \bar{y}) &= \cos 2\pi \left(\frac{j\bar{x}}{N_x} + \frac{k\bar{y}}{N_y} \right), \\ \bar{s}_{j,k}(\bar{x}, \bar{y}) &= \sin 2\pi \left(\frac{j\bar{x}}{N_x} + \frac{k\bar{y}}{N_y} \right). \end{aligned} \quad (24)$$

Equation (23) is just the 2-D discrete Fourier transform of the sampled signal $\bar{h}(\bar{x}, \bar{y})$ and can be calculated rapidly by a fast Fourier transform (FFT) algorithm, implemented for example as `fft2` in the MATLAB language. Spatial frequency components (j, k) have the same meaning in Eqns. (23) and (24) as for the corresponding continuous form expressions $c_{j,k}$ and $s_{j,k}$, with units of ‘cycles per field of view’. One assumption implicit in the use of the 2-D FFT is that the origin of the domain is at the bottom left of the field of view. The shift of the origin to the centre of the domain, as for the two applications considered in the next section, can be achieved by swapping the 4 quadrants of the experimental strain fields, for example with the MATLAB `fftshift` function.

A total of only 4 FFTs are required to assemble all the terms in \mathbf{M} , in which the four functional forms for h are given by the right hand side of Eqns. (19) and (20) as

$$\begin{aligned} h_1(x, y) &= \epsilon_{xx}(x, y) + \epsilon_{yy}(x, y), \\ h_2(x, y) &= \epsilon_{SS}(x, y), \\ h_3(x, y) &= x\epsilon_{SS}(x, y), \\ h_4(x, y) &= y\epsilon_{SS}(x, y). \end{aligned} \quad (25)$$

The computational effort for each 2-D FFT is $O(N_x N_y (\log_2(N_x) + \log_2(N_y)))$ operations, whereas that for assembling the elements of \mathbf{M} from the resulting coefficients is $O(N_F^2) \sim 16N^4$ operations. The latter dominates over the former for problems involving relatively large numbers of Fourier coefficients in the reconstruction. In such cases, the computational effort

becomes essentially independent of the resolution of the experimental strain fields, with a theoretical reduction in computational effort by a factor of $N_x N_y$ by using the fast algorithm over the direct (i.e., element by element) method of assembling the matrix \mathbf{M} . The computational effort for both algorithms scales identically with the number of Fourier terms in the stiffness expansion (i.e., as $O(N_F^2)$), however, since \mathbf{M} is a non-sparse matrix in both cases.

The computation time for the other steps in the algorithm is short compared to that for calculation of \mathbf{M} for the values of N_F used in this paper. The evaluation of the terms in the vector \mathbf{Y} requires $O(N_F)$ operations. The solution of Eqn. (13) by Gaussian elimination requires $O(N_F^3)$ operations. Reconstruction of the elastic stiffness distribution from the solution vector can be handled efficiently by performing a single 2-D inverse Fourier transform on a 2-D array of complex numbers, where the calculated $a_{m,n}$ and $b_{m,n}$ coefficients are the real and imaginary parts, respectively, and requires $O(N_F^2 \log_2(N_F))$ operations. The $O(N_F^3)$ operations required for the Gaussian elimination means that for larger values of N_F , inversion of the matrix could ultimately become the rate-determining step for the algorithm.

For the problem considered in Application 2, the total calculation time for the stiffness identification using the fast algorithm when implemented as a MATLAB script, on an Intel® Core™ i7 CPU 2.79 GHz machine with 8GB of memory, was ~2.5 s and 250 s for problem sizes $N = 20$ and $N = 80$, respectively. This may be compared with values of 6.1×10^3 s and 3.7×10^6 s, respectively, for the direct method. A time saving of 3-4 orders of magnitude is therefore clearly achievable in practice.

3. Validation with numerical data

In this section we give proof-of-principle results from the F-VFM method presented above with spatially-varying stiffness distributions under uniform loading conditions. Three scenarios are considered, one in which the modulus varies smoothly with position, the other two with spatial discontinuities in the modulus. The input data to the F-VFM method were provided by a forward calculation from known stiffness distributions by the finite element method, thus providing a benchmark to compare the reconstructed stiffness maps against.

3.1. Layered-pattern stiffness distribution

A thin rectangular plate of size $L_x \times L_y = 16 \times 10 \text{ mm}^2$ and of thickness $t = 1 \text{ mm}$ containing a discontinuous stiffness distribution pattern, as shown in Fig. 2, was modelled in Mentat2010, the pre/post-processing module of the commercial finite element package MscMarc™2010. The origin of the coordinate system is situated at the centre of the plate. The region of interest was meshed using 1600×1000 linear quadrilateral elements with full integration. The material

was chosen to be linear elastic isotropic, with all elements having the same Poisson's ratio of 0.3 but different reference modulus values of $E = 20$ and 40 MPa. The corresponding reference stiffness values Q_{xx} are therefore 21.98 and 43.96 MPa, respectively (Eqn. (4)). A uniform stress of magnitude $\sigma_{xx} = 1$ MPa pointing outwards was applied horizontally on both vertical edges of the plate.

Figure 2. A rectangular plate with a discontinuous stiffness distribution subject to horizontal uniform stress σ_{xx} .

The three strain field components, ϵ_{xx} , ϵ_{yy} and ϵ_{ss} , provided by the finite element analysis (FEA) were used to calculate the unknown Fourier series coefficients using Eqns. (11) and (13), with the virtual fields from Eqn. (18) and Table **IError! Reference source not found..** In this example, the number of cosine/sine terms in the Fourier series (7) was chosen as $N = 32$, which leads to a total number of unknown Fourier coefficients of $N_F = 2177$ by Eqn. (10). Total computation time for 1600×1000 pixels input strain was $\sim 8.5 \times 10^3$ s on an Intel® Core™ i7 CPU 2.79 GHz machine with 8GB of memory, using the MATLAB programming language with `pinv` operator to perform the inversion of Eqn. (13). Using the fast algorithm to generate the coefficients in the left-hand-side matrix in Eqn. (14) reduced this figure to ~ 20 s.

The reference and recovered stiffness distributions are shown in Fig. 3-a and 3-b. Although the two are seen to be in reasonable overall agreement, the latter is disturbed by a number of vertical ripples. The reason for this disturbance is believed to come from the presence of high frequency terms in the Fourier series of the identifying stiffness Q_{xx} (the number of ripples is equal to N , the number of cosine/sine terms of the selected Fourier series; in this case $N = 32$). To remove such ripples, the recovered stiffness distribution can be smoothed by convolution with an appropriate kernel. Although smoothing is generally undesirable, it is not possible to see finer details in the stiffness reconstruction than pitch value p , as the highest spatial frequency in the reconstructed stiffness maps has pitch $p = \frac{L_x}{N}$ (mm) or $p = \frac{N_\epsilon}{N}$ (pixels) (where N_ϵ is the number of pixels (or sample points/ elements) in the direction along which the ripples are spread). Thus, smoothing with a square kernel of size p , with all points inside the kernel given equal weight, does not significantly degrade spatial resolution beyond the limit already inherent in the technique. It does however result in a narrow ribbon of low magnitude along the edges of the stiffness map as shown in Fig. 3-c. This is due to the fact that any point within a distance $p/2$ from the edge of the map is influenced by the stiffness values outside the region of interest, which are unknown and here assumed to be zero.

The recovered stiffness map after masking out the affected data can be seen in Fig. 3-d. The error map, defined as the difference between the filtered and the reference stiffness distributions, is shown in Fig. 3-e. Figure 3-f shows stiffness profiles at the middle of the stiffness map by plotting a horizontal cross section through the reference stiffness map, the recovered stiffness map and the recovered stiffness map after data smoothing and edge effect masking. It is interesting to observe an overshoot in the recovered stiffness at the transitions

between regions of different modulus, which is analogous to the Gibbs phenomenon when representing discontinuous functions by a Fourier series expansion. Thanks to the smoothing, the influence of this phenomenon is significantly reduced.

Figure 3. Reconstruction of a discontinuous stiffness distribution, with $N = 32$ cosine/sine terms in the Fourier-series stiffness (units: MPa).

3.2. ‘Egg-box’-pattern stiffness distribution

In this section, a second example of the application of the F-VFM is given involving an ‘egg-box’ pattern of spatially varying stiffness distribution. The FE model used to generate the input strain fields consisted of a thin square plate of size $L_x \times L_y = 10 \times 10 \text{ mm}^2$ and of thickness $t = 1 \text{ mm}$. As in the previous section, the geometry was meshed in Mentat2010 using 1000×1000 linear quadrilateral elements with full integration. Two vertical edges of the plate perpendicular to the x -axis were loaded with a uniformly distributed stress $\sigma_{xx} = 1 \text{ MPa}$ pointing outwards. The origin of the coordinate system is at the centre of the plate (see Fig. 4).

The material was chosen to be linear elastic isotropic with the reference elastic modulus distribution given by

$$E = 20 + \cos 2\pi \left(\frac{2x}{L_x} + \frac{y}{L_y} \right) + \sin 2\pi \left(\frac{x}{L_x} + \frac{2y}{L_y} \right) \text{ MPa} \quad (26)$$

and a constant Poisson’s ratio $\nu = 0.3$. Plane stress conditions are applicable in this case since the thickness of the plate is relatively small compared to the other dimensions. The reference stiffness distribution is therefore

$$Q_{xx} = \frac{E}{1-\nu^2} = 21.98 + 1.10 \cos 2\pi \left(\frac{2x}{L_x} + \frac{y}{L_y} \right) + 1.10 \sin 2\pi \left(\frac{x}{L_x} + \frac{2y}{L_y} \right) \text{ MPa} \quad (27)$$

Figure 4. A square plate of ‘egg-box’ stiffness distribution subject to horizontal uniform stress σ_{xx} .

As in the previous section, the strain fields from the forward finite element analysis were used to reconstruct the ‘egg-box’ stiffness distribution. In this example, the number of cosine/sine terms in the Fourier series (Eqn. (7)) is $N = 20$, with a lower limit on the summation over n of 0, and the total number of unknown Fourier coefficients therefore $N_F = 881$ by Eqn. (10).

Some of the main results are shown in Fig. 5. Again ripples in the recovered stiffness map are observed but can be largely removed by smoothing with a uniform square kernel of size equal to the pitch p of the highest frequency ripples. In this case $N_\epsilon = 1000$, $N = 20$ and so $p = \frac{N_\epsilon}{N} = 50$. The edge-effect region of 25 pixels wide (half of the kernel window size) resulting from the convolution is masked out from the reconstructed stiffness as in Fig. 5-c. The residual in

the error map (Fig. 5-d) represents a difference value of about 0.5% between the reference and recovered stiffness distributions.

Figure 5. Reconstruction of an ‘egg-box’ stiffness distribution, with $N = 20$ cosine/sine terms in the Fourier-series stiffness (units: MPa).

3.3. Stiffness distribution with an elastic square inclusion

The third application of the F-VFM is to a thin plate with a square inclusion at the centre. The plate with dimensions of $10 \times 10 \text{ mm}^2$ is uniformly pulled normal to its four edges with a stress value of 1 MPa in magnitude, as shown in Fig. 6. The plate has a Young’s modulus value of 10 MPa and Poisson’s ratio of 0.3. The square inclusion of size $2 \times 2 \text{ mm}^2$, situated at the centre of the plate, is $4 \times$ stiffer than the surrounding material, but has the same Poisson’s ratio.

Figure 6. A thin plate of compliant material (dark grey) containing an elastic square inclusion with stiffness $4 \times$ that of the matrix (light grey), subject to uniform biaxial stress.

A numerical model of the plate was built up with a total of 1000×1000 quadrilateral elements, including 200×200 elements for the inclusion. The strain data obtained from the forward analysis of this model was used in the F-VFM implementation to reconstruct the modulus distribution of the plate. Reconstruction results for the stiffness distribution of the plate are shown in the first row of Fig. 7 for the case $N = 20$. Unlike the two previous examples, negative frequencies were included in the analysis, i.e. the lower limit on n in Eqn. (7) was $-N$ rather than 0. Ripples are visible at the inclusion/matrix boundary which can – as for the layered material in Section 3.1 – be regarded as an example of Gibb’s phenomenon, resulting from the sharp change in modulus between the two phases. Such ripples can be smoothed by convolving the reconstructed stiffness map with a filter of size 50×50 pixels. A horizontal cross section through the middle of the inclusion (Fig. 7-g) shows 4 full sinusoidal waves within the inclusion.

Equivalent stiffness reconstructions for the case $N = 40$ are presented in figures 7-d, -e, -f and -h. Data smoothing is implemented with a filter of 25×25 pixels in this case. Increasing N from 20 to 40 doubles the number of sinusoidal waves within the inclusion, thereby improving the spatial resolution by a factor of $2 \times$ along each axis, and also reduces the width of the low-magnitude border on the stiffness maps.

Figure 7. Reconstruction of a stiffness distribution having an elastic square inclusion, with $N = 20$ and $N = 40$ cosine/sine terms in the Fourier-series stiffness (units: MPa).

4. Sensitivity of the F-VFM to noise

In order to simulate the effect of the noise on the performance of the F-VFM, the numerical input data for Applications 2 and 3 were modified by a number of additive white noise patterns of different standard deviation levels. The noise should not be added directly to the strain fields since the three strains are correlated to each other through the displacement-strain relations. A better way is to introduce the noise into the displacement fields, which also simulates more closely the typical experimental situation, and then calculate the strains from the displacements. Independent random numbers from a zero-mean normal distribution with standard deviation σ were added to the u_x and u_y fields. The algorithm's performance was assessed for ten different σ values ranging from 10^{-3} mm (low noise level) to 10^{-2} mm (high noise level). For comparison, the ranges of displacements (i.e., minimum to maximum across the full field) were 0.593 mm and 0.244 mm for the u_x and u_y fields, respectively of Application 2, with corresponding values of 0.738 mm and 0.738 mm for Application 3. For each of the ten noise levels, 100 noise patterns were generated and the identification of stiffness distribution was therefore carried out a total of 1000 times.

The derivative $\partial u_j / \partial x$ (where $j = x$ or y) at any given point (x, y) was estimated from the u_j values over a square region of size $N_s \times N_s$ pixels centred on (x, y) . A gradient estimator with reduced variance compared to a simple finite difference operator is obtained by least squares fitting a first order polynomial to the displacement data along each row of the square, and then averaging the N_s resulting best-fit gradients over all the rows. The derivative with respect to y was carried out in the same way but with the least squares fitting carried out along the columns of the square and the gradients averaged over the columns. Two kernels of size 7×7 and 13×13 pixels were investigated in Application 2, and 7×7 pixels in Application 3. Both are small compared to the pitch of the highest frequency Fourier coefficient (which is $p = 50$ pixels in Application 2, and $p = 25$ pixels in Application 3) and therefore introduce relatively little additional blurring to the recovered stiffness distribution.

The noisy 'egg-box' strains differentiated with different kernel sizes and at different noise levels are shown in Fig. 8; and the corresponding stiffness distributions recovered by the F-VFM in Fig. 9. It is interesting to note that even though the strain maps are so disturbed at the high noise level that their textures are no longer clearly visible (Fig. 8) compared with the noise-free strain maps, one can still distinctly see the contrast in the identified stiffness after filtering (see Fig. 9).

Figure 8. Numerical strain fields of an 'egg-box' pattern with and without noise addition, differentiated from displacement fields with a gradient kernel size of 13×13 .

Figure 9. Reconstruction of an 'egg-box' stiffness pattern with different strain data shown in figure 8.

The graph in Fig. 10 represents the mean and standard deviation in the average stiffness error in each reconstructed stiffness map at different gradient kernel sizes and noise levels. As would be expected intuitively, at lower noise levels there is less difference in the stiffness residual when using either small or large kernel, with the discrepancies in stiffness residual increasing at higher noise levels. At lower noise level, the mean values of the recovered stiffness seem to be less sensitive to the kernel sizes, but more sensitive to kernel sizes at higher noise levels, as presented by wider error bars.

Figure 10. Sensitivity of the F-VFM to the displacement field noise level and to the strain-evaluation kernel sizes in the identification of an ‘egg-box’ stiffness distribution.

Figure 11 shows another example of the plate with inclusion at medium and high noise levels. A horizontal cross section cutting through the centre of the inclusion shows a stiffness profile not too different from the reference.

Figure 11. Reconstruction of stiffness distribution having an elastic square inclusion at different noise levels of displacement fields.

5. Conclusions and future work

The paper presents a development of the existing virtual fields method by implementing a novel parameterisation of the stiffness distribution with a full 2-D Fourier series expansion. Different stiffness distribution scenarios have been reconstructed after a single computation step without any iteration. The sensitivity of the identification to noise is relatively low (about 5% error with a displacement noise level significantly higher than in typical experimental fields) and the spatial resolution of the recovered stiffness by F-VFM is directly controllable through the choice of maximum spatial frequency. The introduction of the fast algorithm helps reduce computation time by 3-4 orders of magnitude compared with the direct implementation of the F-VFM, allowing problems with up to 1000 degrees of freedom to be solved in just a few seconds on a normal desktop PC.

In this study the reconstructed modulus fields were obtained from the F-VFM under the assumption that the traction distributions are known over the boundaries. In the future the F-VFM will be extended to cope with the cases where boundary conditions are unspecified over at least a part of the boundary of the domain of interest. Other important remaining issues are application of the method to experimental strain fields (as opposed to strain fields calculated by a forward finite element analysis), and extension to the case of anisotropic materials such as carbon-fibre reinforced composites.

References

1. Barbone PE, Oberai AA. Elastic modulus imaging: Some exact solutions of the compressible elastography inverse problem. *Physics in Medicine and Biology* 2007; **52**: 1577-1593.
2. Albocher U, Oberai AA, Barbone PE, Harari I. Adjoint-weighted equation for inverse problems of incompressible plane-stress elasticity. *Computer Methods in Applied Mechanics and Engineering* 2009; **198**: 2412-2420.
3. Banan MR, Hjelmstad KD. Parameter estimation of structures from static response. 2. Numerical simulation studies. *Journal of Structural Engineering-Asce* 1994; **120**: 3259-3283.
4. Doyley MM, Meaney PM, Bamber JC. Evaluation of an iterative reconstruction method for quantitative elastography. *Physics in Medicine and Biology* 2000; **45**: 1521-1540.
5. Koh CG, Perry MJ, Choo YS. Modified genetic algorithm strategy for structural identification. *Computers & Structures* 2006; **84**: 529-540.
6. Xu B, Wu ZS, Chen GD, Yokoyania K. Direct identification of structural parameters from dynamic responses with neural networks. *Engineering Applications of Artificial Intelligence* 2004; **17**: 931-943.
7. Avril S, Huntley JM, Pierron F, Steele DD. 3D heterogeneous stiffness reconstruction using MRI and the virtual fields method. *Experimental Mechanics* 2008; **48**: 479-494.
8. Pierron F, Grédiac M. *The Virtual Fields Method: Extracting constitutive mechanical parameters from full-field deformation measurements*. Springer New York, 2012;536.
9. Avril S, Grédiac M, Pierron F. Sensitivity of the virtual fields method to noisy data. *Computational Mechanics* 2004; **34**: 439-452.
10. Grédiac M, Toussaint E, Pierron F. Special virtual fields for the direct determination of material parameters with the virtual fields method. 1 - Principle and definition. *International Journal of Solids and Structures* 2002; **39**: 2691-2705.
11. Pierron F, Grédiac M. A T-shaped specimen for the direct characterization of orthotropic materials. *International Journal for Numerical Methods in Engineering* 1998; **41**: 293-309.
12. Toussaint E, Grédiac M, Pierron F. The virtual fields method with piecewise virtual fields. *International Journal of Mechanical Sciences* 2006; **48**: 256-264.
13. Kim JH, Pierron F, Wisnom MR, Syed-Muhamad K. Identification of the local stiffness reduction of a damaged composite plate using the virtual fields method. *Composites Part A-Applied Science and Manufacturing* 2007; **38**: 2065-2075.
14. Bower AF. *Applied Mechanics of Solids*. CRC Press, 2010.
15. Kim JH. Identification of the local stiffness reduction of a damaged composite plate using the virtual fields method 2008; **PhD Thesis**.
16. Avril S, Bonnet M, Bretelle A, Grédiac M, Hild F, Ienny P, Latourte F, Lemosse D, Pagano S, Pagnacco E, Pierron F. Overview of identification methods of mechanical parameters based on full-field measurements. *Experimental Mechanics* 2008; **48**: 381-402.
17. Le Louëdec G, Sutton MA, Pierron F, Reynolds AP. Dynamic local elasto-plastic identification of the behaviour of aluminium FSW welds with the virtual fields method. *Applied Mechanics and Materials* 2011; **70**: 135-140.
18. Sutton MA, Yan JH, Avril S, Pierron F, Adeeb SM. Identification of heterogeneous constitutive parameters in a welded specimen: Uniform stress and virtual fields methods for material property estimation. *Experimental Mechanics* 2008; **48**: 451-464.

19. Tattoli F, Pierron F, Rotinat R, Casavola C, Pappalettere C. Full-field strain measurement on titanium welds and local elasto-plastic identification with the virtual fields method. *International Conference on Advances in Materials and Processing Technologies, Pts One and Two* 2010; **1315**: 860-865.
20. Kreyszig E. *Advanced Engineering Mathematics*. John Wiley & Sons, Inc., 2006.

Table I. Virtual displacement field components u_x^* and u_y^* and their derivatives.

Sub-matrix	p	u_x^*	$\frac{\partial u_x^*}{\partial x}$	$\frac{\partial u_x^*}{\partial y}$	q	u_y^*	$\frac{\partial u_y^*}{\partial x}$	$\frac{\partial u_y^*}{\partial y}$
A,B	0	$xc_{0,q}$	$c_{0,q}$	$-\frac{2\pi q}{L_y}xs_{0,q}$	0	$yc_{p,0}$	$-\frac{2\pi p}{L_x}ys_{p,0}$	$c_{p,0}$
	> 0	$\frac{L_x}{2\pi p}s_{p,q}$	$c_{p,q}$	$\frac{L_x q}{L_y p}c_{p,q}$	$\neq 0$	$\frac{L_y}{2\pi q}s_{p,q}$	$\frac{L_y p}{L_x q}c_{p,q}$	$c_{p,q}$
C,D	0	$xs_{0,q}$	$s_{0,q}$	$\frac{2\pi q}{L_y}xc_{0,q}$	0	$ys_{p,0}$	$\frac{2\pi p}{L_x}yc_{p,0}$	$s_{p,0}$
	> 0	$-\frac{L_x}{2\pi p}c_{p,q}$	$s_{p,q}$	$\frac{L_x q}{L_y p}s_{p,q}$	$\neq 0$	$-\frac{L_y}{2\pi q}c_{p,q}$	$\frac{L_y p}{L_x q}s_{p,q}$	$s_{p,q}$

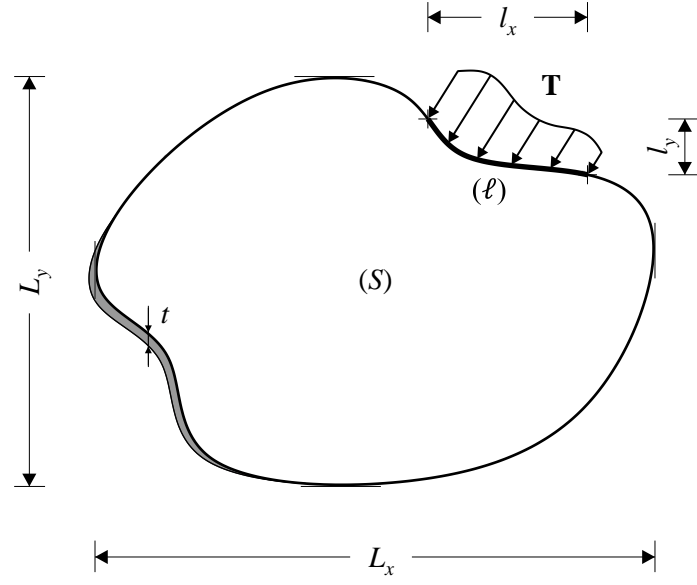


Figure 1. A thin structure of arbitrary shape subject to a traction distribution \mathbf{T} on a portion (ℓ) of the boundary. Dimensions of the domain of interest (S) are denoted by L_x and L_y whilst those of the traction boundary are l_x and l_y . The properties are assumed constant through the nominal thickness t of the structure.

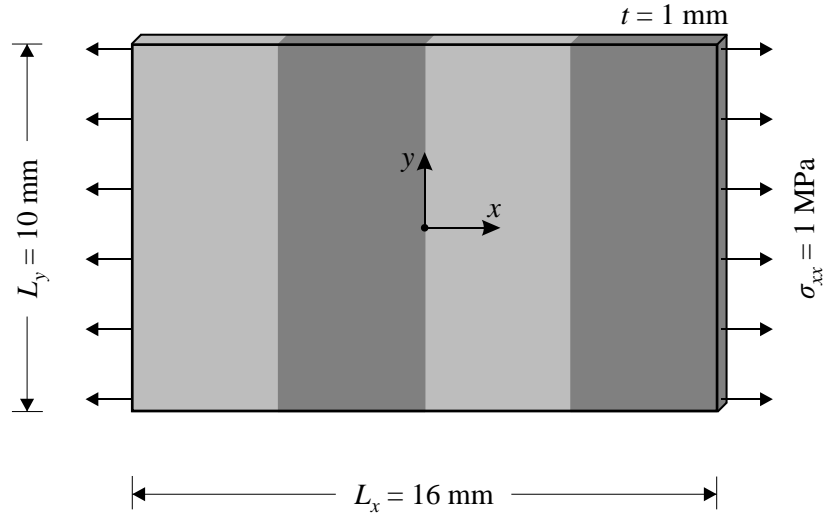


Figure 2. A rectangular plate of a discontinuous stiffness distribution subject to horizontal uniform stress σ_{xx} . The reference elastic modulus E takes the values of 20 MPa (dark grey) and 40 MPa (light grey) on different portion of the plate. Corresponding reference stiffness values are 21.98 MPa and 43.86 MPa, respectively. The origin of the coordinate system is at the centre of the plate.

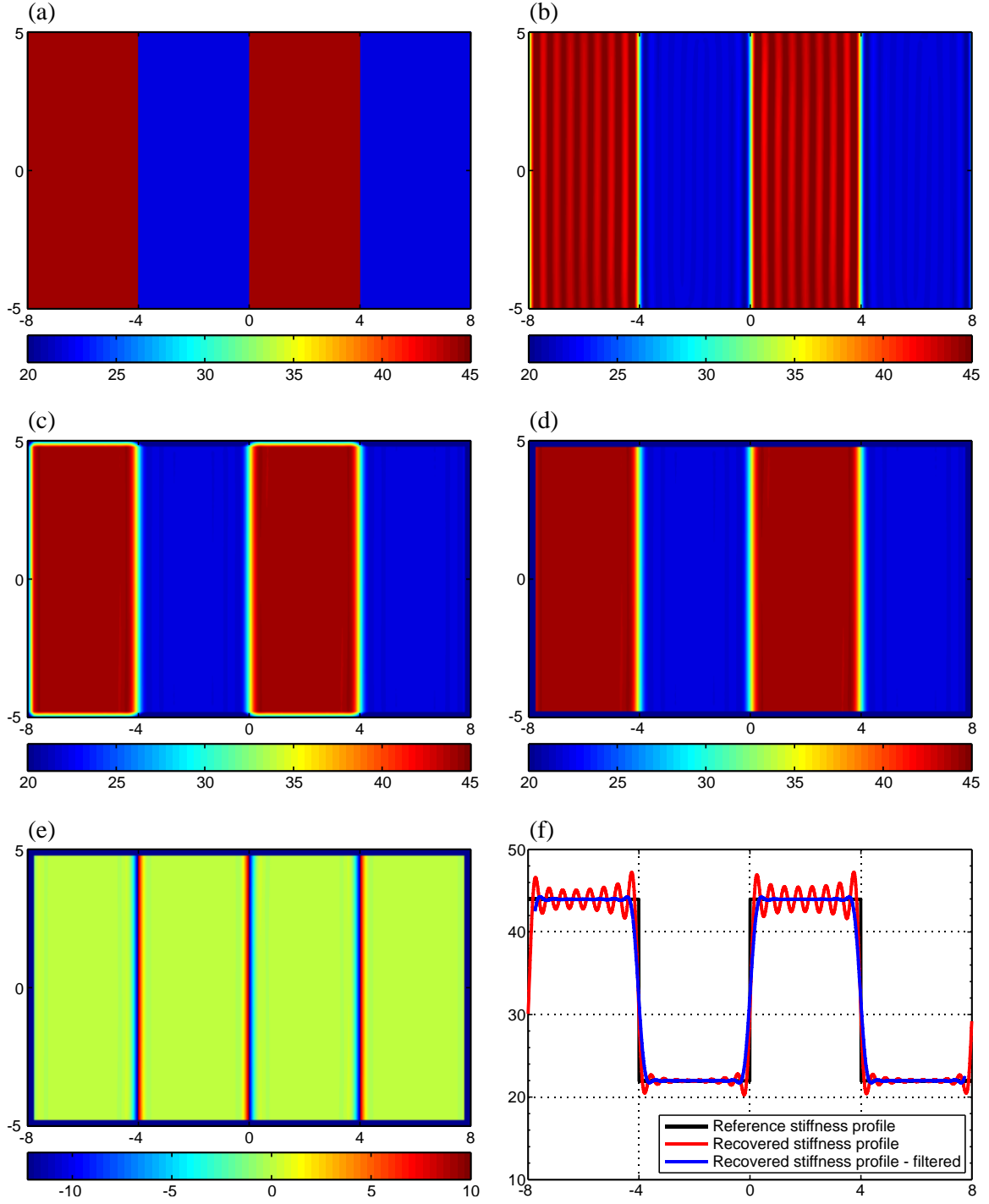


Figure 3. Reconstruction of a discontinuous stiffness distribution, with $N = 32$ cosine/sine terms in the Fourier-series stiffness (units: MPa). (a) Reference stiffness distribution (mesh size 1600×1000); (b) Recovered stiffness distribution by F-VFM; (c) Recovered stiffness in (b) after smoothing by an average filter of size 50×50 pixels; (d) Recovered stiffness in (c) after masking out outlier data near the edges; (e) Stiffness error map (difference between the stiffness maps in (a) and (d)); (f) A horizontal stiffness profile drawn through the middle of the domain (vertical axis: Stiffness / MPa, horizontal axis: x / mm).

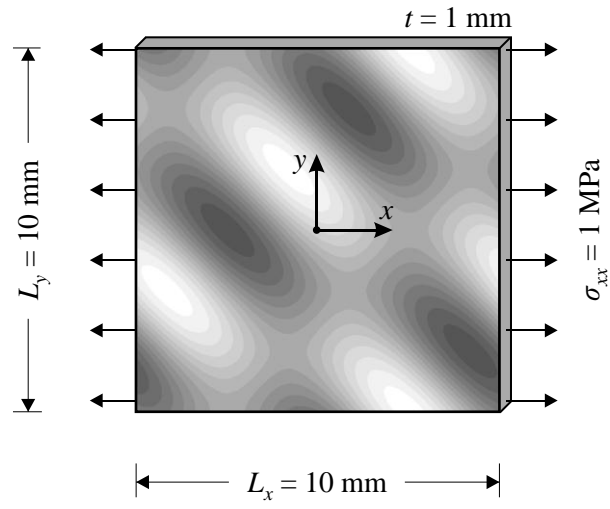


Figure 4. A square plate of an ‘egg-box’ stiffness distribution subject to horizontal uniform stress σ_{xx} .

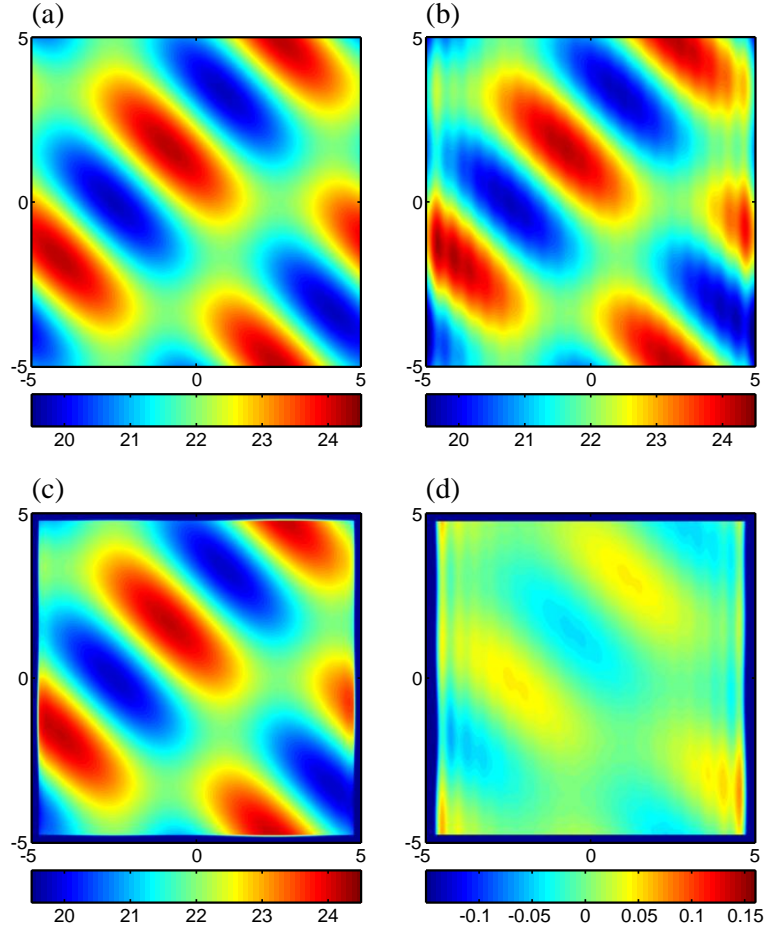


Figure 5. Reconstruction of an ‘egg-box’ stiffness distribution, with $N = 20$ cosine/sine terms in the Fourier-series stiffness (units: MPa). (a) Reference stiffness distribution (1000×1000 pixels); (b) Recovered stiffness distribution by F-VFM; (c) Recovered stiffness in (b) after smoothing by an average filter of size 50×50 pixels; (d) Stiffness error map (difference between the reference and the recovered stiffness after data smoothing and masking out redundant data near the edges).

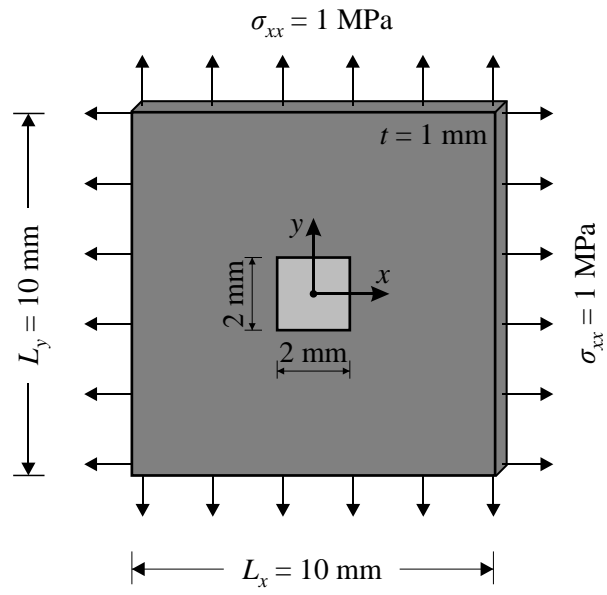


Figure 6. A thin plate of compliant material (dark grey) containing an elastic square inclusion with stiffness $4\times$ higher (light grey), subject to uniform biaxial stress.

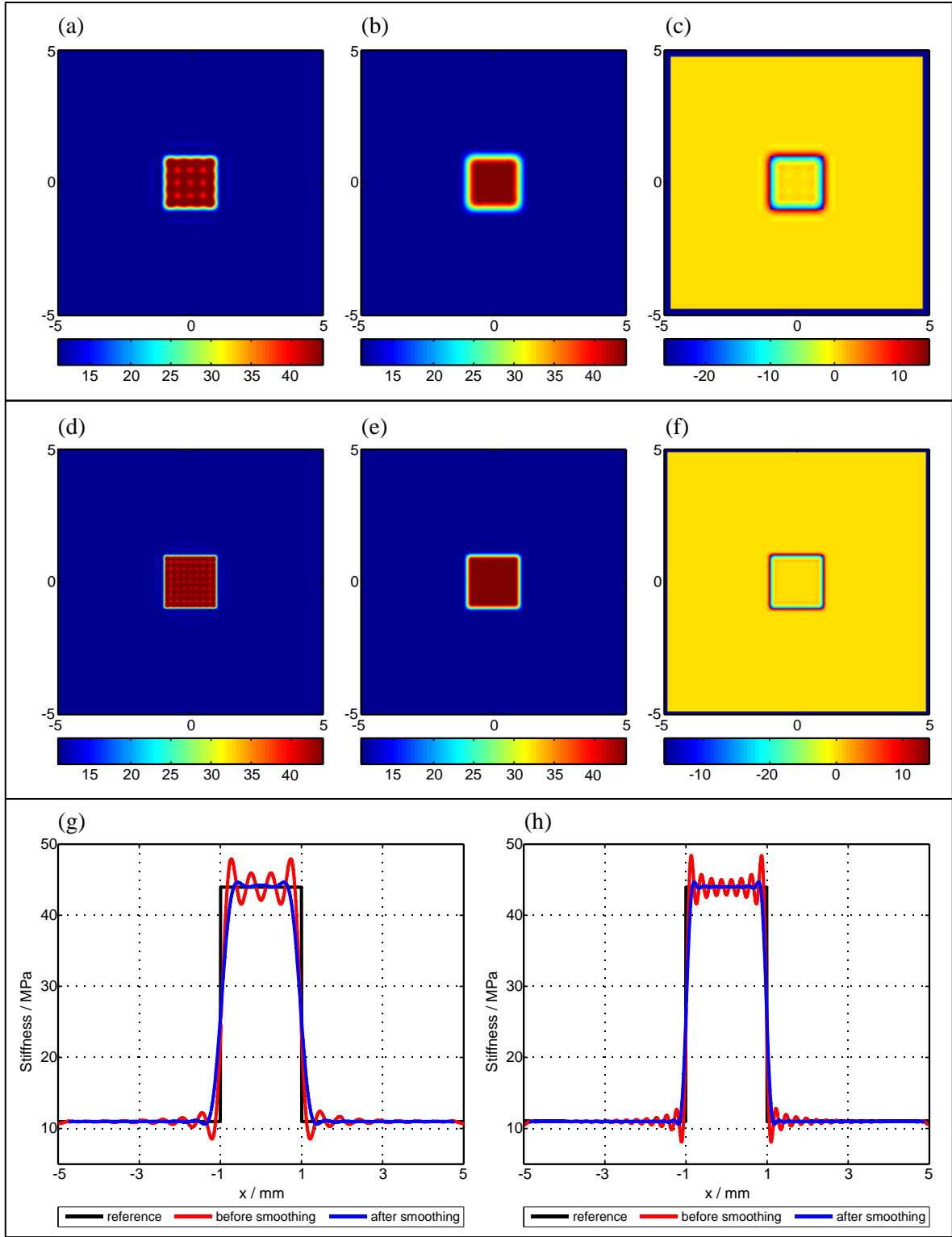


Figure 7. Reconstruction of a stiffness distribution from sample with a square inclusion, with $N = 20$ (top row) and $N = 40$ (middle row) (units: MPa). (a),(d): Recovered stiffness distribution by F-VFM; (b),(e): as for (a),(d) after smoothing by a moving average filter of size 50×50 and 25×25 pixels, respectively, and masking out outlier data near the edges; (c),(f): stiffness error map (difference between (b),(e) and the reference); (g),(h) horizontal cross sections through the centre of the inclusion for $N = 20$ and $N = 40$, respectively, compared with the reference.

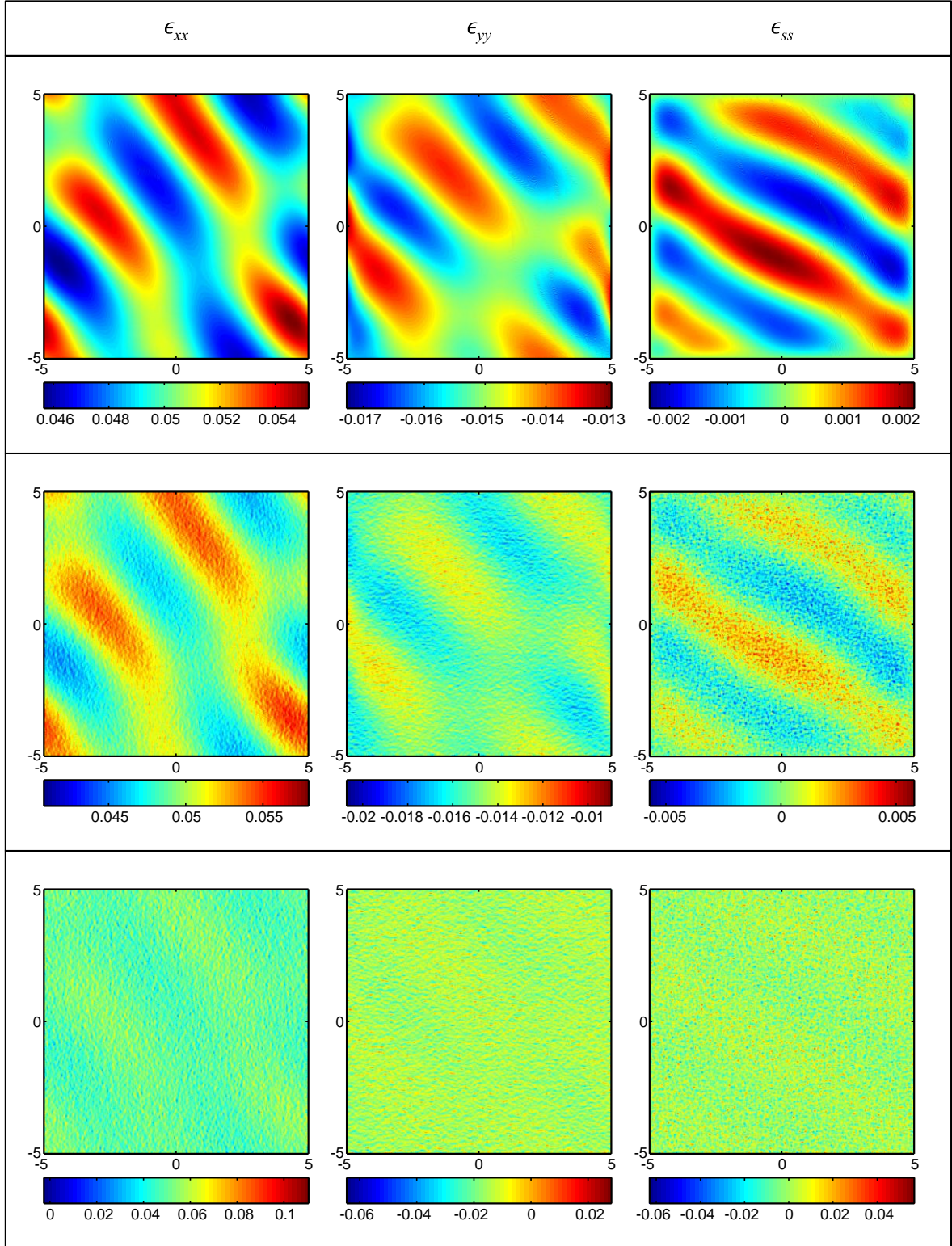


Figure 8. Numerical strain fields of an ‘egg-box’ pattern obtained from a forward finite element analysis, differentiated from displacement fields with a gradient kernel size of 13×13 pixels, with and without the presence of noise. The three strain fields, ϵ_{xx} , ϵ_{yy} and ϵ_{ss} fields are shown respectively in the left, middle and right hand columns of the figure. Figures in the top row are noise-free, in the

middle row are with displacement noise level $\sigma = 10^{-3}$ mm (low noise level), and in bottom row with $\sigma = 10^{-2}$ mm (high noise level).

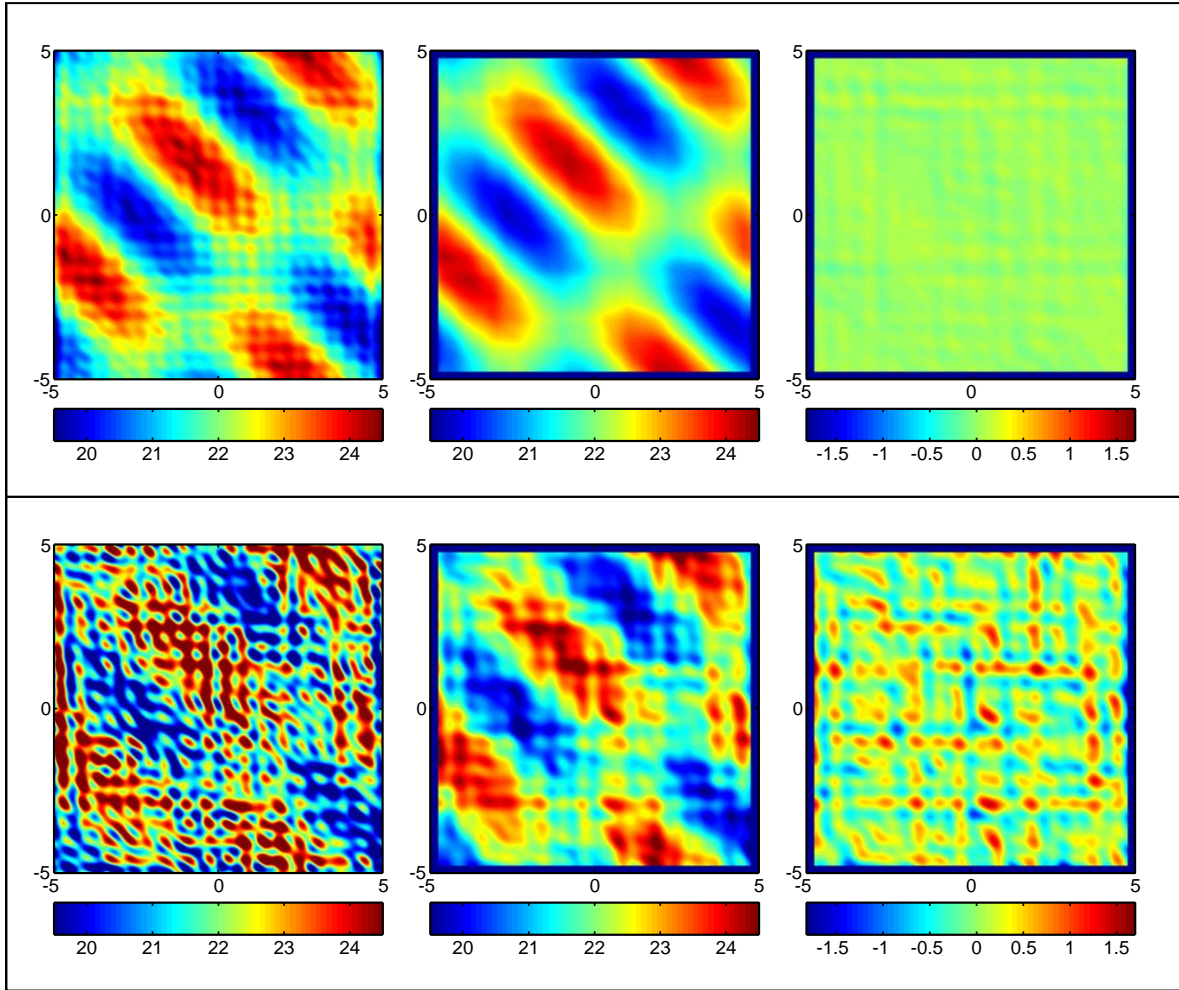


Figure 9. Reconstruction of an ‘egg-box’ stiffness pattern with different strain data shown in figure 8. Figures in the left column are the reconstructed stiffness patterns by the F-VFM with different noise levels, in the middle columns are distributions after data smoothing/removing, and in the right column are error of the recovered stiffness with respect to the reference. Different noise levels are added to displacement fields: $\sigma = 10^{-3}$ mm (top row) and $\sigma = 10^{-2}$ mm (bottom row). Displacement gradient kernel size = 13×13 pixels throughout.

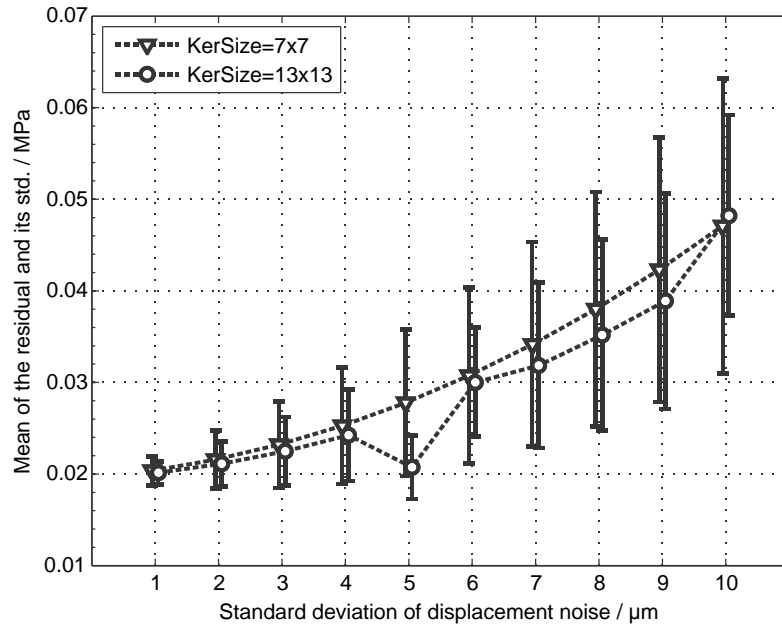


Figure 10. Sensitivity of the F-VFM to the noise levels of displacement fields and to the strain-evaluation kernel sizes in the identification of an ‘egg-box’ stiffness distribution.

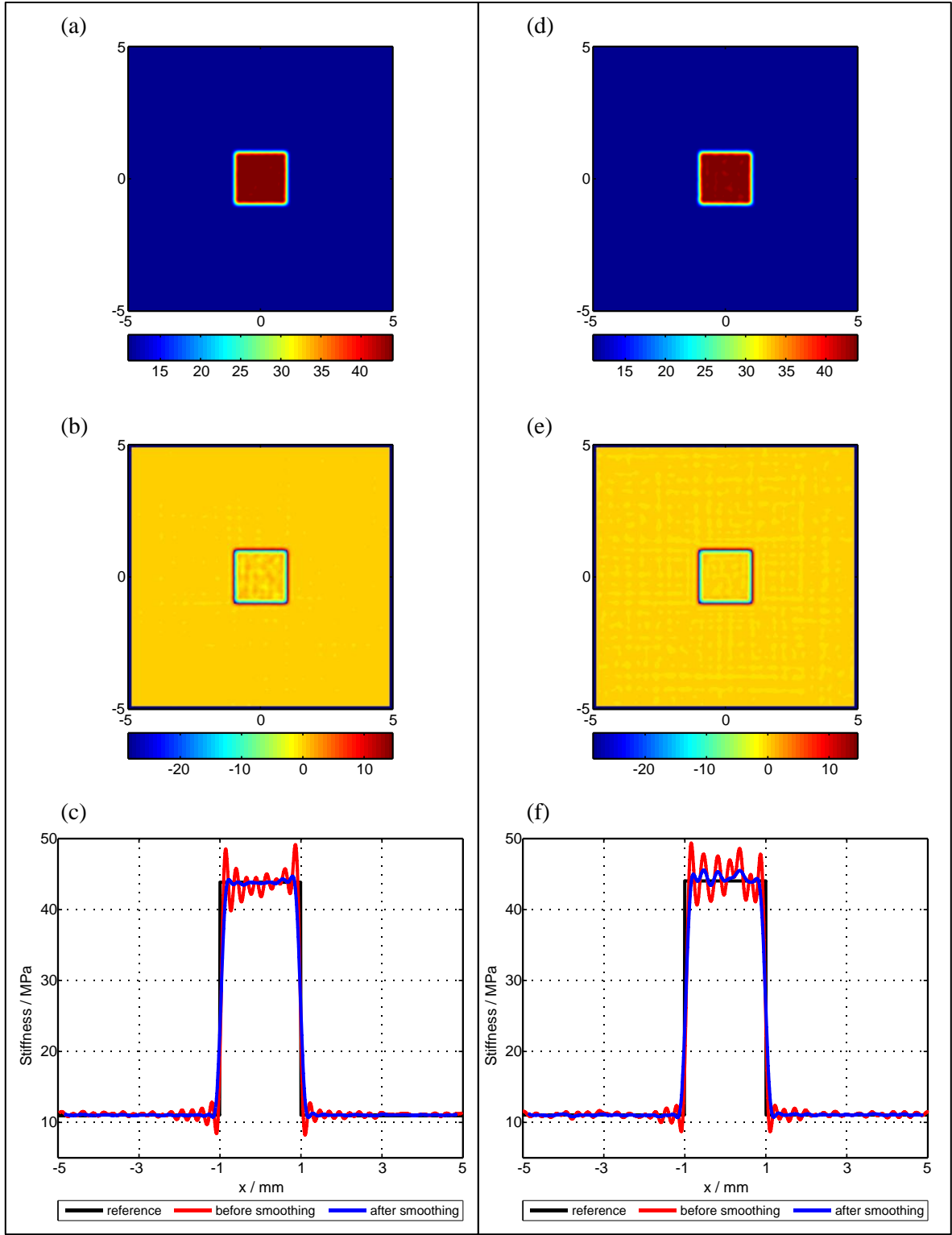


Figure 11. Reconstruction of stiffness distribution for the elastic square inclusion at different noise levels in the displacement fields: $\sigma = 5 \times 10^{-3}$ mm (left column) and $\sigma = 10^{-2}$ mm (right column). The F-VFM was implemented with $N = 40$, and with a displacement-gradient kernel size of 7×7 pixels throughout. (a),(d): Recovered stiffness distribution by F-VFM after data smoothing and filtering; (b),(e): Stiffness error map (difference between the stiffness maps in (a),(d) and the reference); (c),(f)

horizontal cross sections through the centre of the inclusion for $\sigma = 5 \times 10^{-3}$ mm and $\sigma = 10^{-2}$ mm, respectively, compared with the reference.